Applied Surface Science 664 (2024) 160272

Contents lists available at ScienceDirect

Applied Surface Science

journal homepage: www.elsevier.com/locate/apsusc

Full Length Article

Influence of Nb substrate morphology and atomic structure on Sn nucleation and early Nb_3Sn growth

Sarah A. Willson, Helena Lew-Kiedrowska, Van Do, S.J. Sibener *

The James Franck Institute and Department of Chemistry, The University of Chicago 929 E. 57th Street, Chicago, IL 60637, USA

ARTICLE INFO

Keywords:
Nb_3Sn
Superconductor
Film growth
Metal oxide
Vapor deposition
SRF

ABSTRACT

The enhanced accelerating performance of Nb_3Sn-coated Nb superconducting radio frequency (SRF) cavities is severely limited by quenching sites at material defects formed during the Nb_3Sn film growth procedure. In this work, we aimed to understand the complex surface-mediated interactions that drive initial Nb_3Sn formation during the Sn vapor deposition procedure used to fabricate Nb_3Sn coated SRF cavities. Nb substrates were modified, coated with Sn, and then characterized using an ultra-high vacuum (UHV) chamber equipped with metal deposition and *in situ* surface analysis capabilities. The atomic structure of the Nb oxide surface was modified to assess how the Nb surface defect density and crystallographic orientation impact the size of nucleated Sn islands and relative Nb_3Sn growth rates. Formed Nb_3Sn/Nb surfaces were visualized using *ex situ* scanning electron microscopy (SEM) and post-deposition annealing revealed Sn desorption and Nb_3Sn degradation pathways. Finally, we showed that the Sn deposition conditions can be modified to overcome the growth barriers that are imposed by the Nb morphology. This study provides a unique bridge between fundamental growth studies in pristine conditions with observed phenomena of Nb_3Sn grown on realistic cavity surfaces.

1. Introduction

High-performance linear particle accelerator facilities use niobium (Nb) SRF cavities to produce powerful beams. The high critical temperature (T_C: ~ 9 K) and quality factor (Q) at $T_{operation}$ ~ 2 K justifies Nb as the standard cavity material [1–3]. To achieve higher accelerating gradients and reduce the cryogenic burden during operation, efforts are underway to enhance the performance of Nb SRF cavities [4]. One promising SRF material is the Nb_3Sn alloy, which has a significantly higher T_C (~18 K) and superheating field than Nb [5]. The brittle properties of Nb_3Sn limit its use in SRF as a coating material on the interior of existing Nb cavities. The typical thickness of the Nb_3Sn coatings is ~ 1-μm in order to limit RF penetration at the intermetallic interface. It was estimated that a Nb cavity coated with a pristine Nb_3Sn film will enable SRF operation at 4 K with comparable Q factors [6].

However, Nb_3Sn coated SRF cavities have not achieved the high predicted Q factors. This has largely been attributed to material defects in the grown Nb_3Sn film [7]. These defects include areas of poor film growth, Sn stoichiometric deficiencies, excess surface roughness, and segregated Sn [8,9]. The standard procedure for growing Nb_3Sn coatings on the interior of the Nb SRF cavity is through a Sn vapor deposition and infusion process. During growth, a Sn source is inserted into the Nb cavity, and both the cavity and Sn are independently heated inside a furnace. The deposition process starts with a lower temperature nucleation step (typical T_{Nb}: 500 °C) followed by a coating stage (typical T_{Nb}: 1100 °C) [10]. $SnCl_2$ is commonly added during the nucleation step to enhance the Sn vapor pressure. In recent years, significant progress has been made towards studying and optimizing this growth process [4,11].

One such area of progress is identifying the relatively slow diffusion of bulk Sn through Nb_3Sn causing extensive Sn deficiencies on larger Nb_3Sn grains. It has been demonstrated that smaller grain Nb_3Sn films with higher grain boundary densities suffer much fewer Sn deficiencies, supporting the view that Sn grain boundary diffusion is the dominant growth process [12,13]. One remaining issue regarding Sn diffusion, however, is the persistence of segregated Sn on the Nb_3Sn surface. Residual Sn islands on Nb_3Sn have been observed and identified as a major limiting factor in the Q slope of Nb_3Sn coated cavities [14,15]. At the same time, the propensity for Sn precipitation and desorption from Nb_3Sn surfaces is also a significant issue during material preparation. There lacks a thorough understanding of how the delicate balance of Sn incorporation, surface aggregation, and desorption rates can be optimized by modifying the relative Sn deposition and Nb substrate

* Corresponding author.
E-mail address: s-sibener@uchicago.edu (S.J. Sibener).

https://doi.org/10.1016/j.apsusc.2024.160272
Received 20 March 2024; Received in revised form 29 April 2024; Accepted 11 May 2024
Available online 12 May 2024

temperatures during growth.

Beyond the complexity introduced by the competing thermally activated Sn processes, the Nb surface itself plays a major role in driving Nb_3Sn growth. The influence of the Nb substrate morphology is potentially the least understood when considering all the relevant parameters during the vapor deposition process. This is in part due to the highly reactive nature of the Nb surface. Nb forms a ~ 5 nm native oxide, largely composed of the pentoxide (Nb_2O_5) phase with trace monoxide (NbO) and dioxide (NbO_2) components at the metallic interface. Upon annealing above ~ 300 °C, rapid dissolution of the native oxide leaves a ~ 2 monolayer (ML) NbO phase [3]. This NbO is highly resistant to thermal reduction and requires temperatures above 2000 °C to achieve the metallic Nb surface. Chemical alterations to the Nb surface significantly impact Nb_3Sn growth. Increasing the native oxide thickness *via* anodization is a now institutionalized step in the standard Nb_3Sn growth procedure. Increasing the native oxide thickness was associated with the formation of a more uniform film, but it is not clear whether the oxygen content at the Nb surface aids in stabilizing the intermetallic interface [12,16,17]. However, the oxygen dissolution rate at the Sn nucleation substrate temperatures (500 °C) suggests that a NbO surface oxidation state is formed under these conditions, even for the thicker pre-anodized Nb_2O_5 surfaces [18–20]. Literature has shown that the formation of the Nb_2O_5 layer results from the injection of oxygen into the metallic Nb; this process exacerbates existing Nb surface defects, creating deep serrations at the metallic Nb interface [21]. The NbO surface formed by annealing the native oxide to lower temperatures has distinct surface sites and mass density, due to the relatively slow Nb mass transport at 900 °C [18].

Beyond the Nb oxidation state, it is also poorly understood how other Nb structural properties influence Sn nucleation [7]. Previous work has suggested that Nb_3Sn films grown on Nb(1 1 1) are patchier than Nb_3Sn films grown on Nb(1 0 0) or Nb(1 1 0) [22]. However, it is not known whether the patchy growth on Nb(1 1 1) results from the lattice strain at an Nb_3Sn/Nb(1 1 1) interface or whether the Sn nucleation is less favorable on certain Nb orientations. During polycrystalline film growth at a high temperature, the adatom behavior is influenced by competing lateral diffusion, desorption, and film incorporation rates. Generally, the critical nucleation size and lateral diffusivity of metal adsorbates on metal oxide surfaces depend on the crystallographic orientation and step edge density of the substrate [23].

The work presented herein examines how the Nb substrate facilitates Sn nucleation and initial Nb_3Sn formation. 10 nm of Sn was evaporated onto a Nb substrate with a range of Nb substrate properties and Sn deposition conditions. Nb substrates were prepared, characterized, and coated all in an *in situ* UHV chamber. The formed Nb_3Sn/Nb surfaces were characterized using *in situ* Auger electron spectroscopy (AES) and x-ray photoelectron spectroscopy (XPS), giving unique insight towards the Nb-Sn-O interactions without the influence of atmospheric exposure. After stopping the Nb_3Sn growth relatively early in the process, we used *ex situ* SEM and energy dispersive x-ray spectroscopy (EDS) to visualize the energetically favorable diffusion pathways that dictate the eventual homogeneity of the fully formed Nb_3Sn film. Growth on polished Nb single crystal surfaces isolated the Sn surface behavior from the influence of Nb grain boundaries and larger scale defects. To better represent the surfaces of Nb SRF cavities, Nb_3Sn films were then grown on polycrystalline Nb with different initial surface oxides. The initial Nb oxidization state was shown to reduce the Sn nucleation barrier, not due to the oxygen content, but from the binding site landscape determined by the surface defect density. Following deposition, SEM, EDS, and XPS characterization of annealed Nb_3Sn/Nb surfaces revealed the film degradation pathways and the relative thermal stability of Sn species on the Nb surface. Finally, Sn was deposited on polycrystalline Nb at a higher growth rate and deposition temperature to demonstrate how the diffusion barriers imposed by the Nb substrate can be overcome using improved growth conditions. These results collectively highlight the significance of the Nb substrate morphology in driving Nb_3Sn nucleation. These growth experiments provide a unique glimpse into the early Sn nucleation process on a dynamic and complex Nb surface.

2. Experimental methods

Modifications to the Nb substrate were conducted in UHV chamber containing a preparation/analysis chamber (base pressure: $< 1 \times 10^{-10}$ torr) and a metal deposition chamber (base pressure: $< 1 \times 10^{-9}$ torr, base pressure, during deposition: $\sim 5 \times 10^{-9}$ torr). Sn deposition experiments were performed on both polycrystalline and single crystal Nb samples. Polycrystalline samples (99.9 % purity, 10 mm diameter, Goodfellow) did not undergo any polishing procedure and had a roughness of $R_a \sim 0.09$ μm. Nb(1 0 0), Nb(1 1 0), and Nb(1 1 1) single crystals (99.99 % purity, 10 mm diameter, Surface Preparation Laboratory) were mechanically polished to $R_a < 0.03$ μm. To reduce carbon contamination, all Nb samples were subjected to multiple cycles of Ar^+ sputtering (1.5 keV) and electron-beam annealing (T_{anneal}: 1630–1670 °C) under UHV before any additional surface modifications were carried out. The Nb temperature was monitored using an infrared pyrometer (Mikron Infrared, MG-140).

To prepare the Nb surface, we relied on previously established procedures for varying the NbO surface structure [24,25]. Despite any oxidation or sputtering steps, it is important to note that Nb will form a persistent NbO surface termination > 300 °C. Due to the relatively slow Nb diffusion rate compared to O in Nb oxide layers, any changes in the initial Nb oxidation will ultimately vary the local surface sites during the heated Sn exposure without deviating from the NbO chemical state [19]. The low-defect density NbO surface was formed by annealing to a higher temperature before the Sn deposition (T_{anneal}: 1630 °C) [26]. At these annealing temperatures, NbO surfaces form ordered reconstructions on multiple crystallographic orientations [25,27]. Notably, the oxygen content and structure of the (3 × 1)-O reconstruction that forms on Nb (1 0 0) is stable even at elevated temperatures [28].

To form the native Nb_2O_5, a clean NbO surface was exposed to atmosphere in the UHV load lock chamber for 5 min. The load lock chamber door was opened slightly to prevent carbon contamination, which was confirmed by AES/XPS analysis. Before Sn exposure, the formed Nb_2O_5 surface was heated to the deposition temperature (T_{dep}: 850 °C), during which the Nb_2O_5 surface was reduced to NbO. However, heating the native oxide surface to only 850 °C is not sufficient to form the more ordered NbO reconstructions, leaving a NbO surface termination with a greater concentration of stable Sn binding sites [25]. Since the temperature of the Sn source is independently controlled, the Nb substrate was able to reach this deposition temperature before any Sn vapor was introduced.

The Nb_3Sn coating was formed in an *in situ* metal deposition chamber equipped with a sample stage that enables electron-beam annealing of the Nb substrate during deposition. Sn pellets (99.998 %, Kurt Lesker) were evaporated from a crucible inside an electron beam evaporator (EFM3T, Focus GmbH). The Sn was thoroughly degassed before any evaporation. The Sn temperature, or Sn evaporation rate, was monitored using an internal flux monitor inside the evaporator. The Sn deposition rate was calibrated with sub-nm precision using a quartz crystal microbalance (QCM, INFICON). The calculated Sn deposition rates and coverages were confirmed with scanning tunneling microscopy (STM) and AES at near monolayer (ML) coverages. A linear relationship was established between the evaporator flux monitor and the Sn deposition rate. Directly following deposition, *in situ* AES and XPS spectra of the coated Nb samples were taken. A 3.00 keV electron source was used in AES and a Mg Kα photon source (Specs XR 50) was used for XPS. Both AES and XPS photoelectron signals were collected using a cylindrical mirror analyzer (Staib DESA 100). The Mg anode x-ray source has a 0.34 eV half width at half maximum (HWHM) and a ~ 6 mm diameter spot size.

SEM (Zeiss Merlin) and EDS (Oxford Ultim Max 100) data of the Nb_3Sn films were taken *ex situ*. SEM images were taken using the

Everhart Thornley secondary electron (SE), In-lens SE, In-lens energy selective Backscatter (EsB), and angle selective Backscatter (AsB) detectors. The primary beam was between 1–7 keV during SEM analysis and kept at 7 keV during EDS acquisition. The typical primary beam current was 5 nA. Quantifying the Nb_3Sn domain distributions and Sn island sizes from the SEM images was done using the Gwyddion software. X-ray diffraction (XRD, Rigaku SmartLab) confirmed the formation of the A15 Nb_3Sn crystal structure [29]. To test the thermal stability of the formed Nb_3Sn layers, the samples were returned to the UHV chamber to undergo annealing experiments at T_{anneal} = 850, 925, 1000, and 1100 °C for 60 min. XPS and AES spectra were taken following these anneals. Background subtraction of XPS data was done in CasaXPS software and peak fitting was done with the Igor XPST 1.3 Fit Assistant (WaveMetrics, Inc.).

3. Results and Discussion

A summary of the parameters held constant and changed for each experiment can be found in Table 1. The total amount of evaporated Sn was 10 nm in each experiment. **Sections 3.1-3.3** of the **Results and Discussion** address how changing Nb substrate properties impact Nb_3Sn growth while keeping the deposition conditions the same in each experiment. A low Nb_3Sn growth rate of 0.44 nm/min was used in these experiments. This relatively low growth rate was selected for these experiments to promote the Sn-deficient growth pathways that are often associated with poor Nb_3Sn film growth. Intentionally depositing Sn at these suboptimal conditions will enable us to visualize how the Nb substrate participates in limiting early film growth. The standard Nb temperature during deposition was 850 °C. This temperature was selected to limit Sn desorption while also suppressing the formation of any alternative Nb-Sn intermetallic species [5,24]. **Section 3.3** shows the impact of annealing the films formed in **Section 3.2**. SEM, EDS, and XPS data are shown at successive annealing temperatures as the Nb_3Sn degrades due to Sn precipitation and desorption. Finally, **Section 3.4** shows how optimizing our deposition conditions, by increasing the growth rate and T_{dep}, can overcome many of the growth barriers imposed by the Nb substrate.

3.1. Nb_3Sn growth on Nb(100), Nb(110), and Nb(111)

SEM images of the Nb_3Sn/Nb surfaces formed following Sn deposited on Nb(100), Nb(110), and Nb(111) single crystals are shown in Fig. 1. The Nb crystals were polished and prepared with an initial Nb_2O_5 surface before Sn deposition at 850 °C with a 0.44 nm/min growth rate. The average Nb_3Sn nucleation density and domain area are plotted on a log scale in Fig. 1**(d)**. The highest density of Nb_3Sn nucleation sites formed on Nb(100) as compared to the films grown on Nb(110) and Nb(111). Across the Nb(100) crystal, the density and appearance of Nb_3Sn domains were consistent, with 105 Nb_3Sn nucleation sites formed per square millimeter. Each Nb_3Sn nucleation site formed on Nb(100) typically contained between 2–8 growth Nb_3Sn domains. These Nb_3Sn domains on Nb(100) had a high degree of rotational symmetry with respect to the other domains at each shared nucleation site. The yellow arrows in Fig. 1**(a)** show an example of multiple domain growth directions emerging from a single nucleation site on Nb(100). The arrows orientated on individual Nb_3Sn domains also denote the preferred growth rate in the direction away from the shared nucleation site, producing petal-shaped domains with a high aspect ratio. The oblong shape of the Nb_3Sn domains may be due to low Sn diffusivity, favoring kinetically favored growth pathways [30]. Literature has shown that the initial Nb_3Sn growth rate is diffusion-limited, supporting that Nb_3Sn growth is heavily driven by the nucleation and availability of Sn islands [7,30,31]. Sn clusters were observed near the Nb_3Sn/Nb(100) film edges (Fig. 1**(b)**). However, these Sn islands do appear to be preferentially attached to defect sites on the Nb(100) surface, likely corresponding to step edges of the ~ 100 nm wide terraces.

Sn deposition on Nb(110) (Fig. 1**(c)**) resulted in a similar Nb_3Sn film coverage as on Nb(100), but formed only 1.5 Nb_3Sn nucleation sites per square millimeter. The area of each Nb_3Sn domain on Nb(110) was significantly larger compared to those formed on Nb(100). The Nb_3Sn growth on Nb(110) also had a stronger degree of radial uniformity, producing rounder domains that coalesced leaving no exposed Nb(110) substrate. The lack of preferential growth directions suggests that the Nb_3Sn on Nb(110) followed a more thermodynamically favorable route than on Nb(100) [30]. This is supported by the smaller Sn islands adsorbed on Nb(110) near the film edges (Fig. 1**(d)**). Generally, the diffusion coefficient, D, for adsorbed metal clusters decreases with respect to the island radius, r, as shown in **Eq. (1)**,

$$D \propto r^{-x} e^{\frac{-E_S(r)}{kT}} \quad (1)$$

where E_S is a lateral diffusion energy term that is inversely related to r [32]. x is a constant typically between 1–3, depending on the diffusion mechanisms [33,34]. Based on, **Equation (1),** the smaller Sn islands on Nb(110) have a higher diffusivity than the larger Sn on Nb(100). A reduced Sn diffusion barrier at the film growth front, may in part, explain the higher Nb_3Sn growth rate observed on Nb(110). Overall, the Nb_3Sn formed the largest domains on Nb(110), suggesting that Nb (110) may be prone to forming Sn-deficiencies during the later growth stages due to the relatively slow Sn diffusion through bulk Nb_3Sn [7].

The least Nb_3Sn growth occurred on Nb(111). Across the entire Nb (111) crystal, only three nucleation sites were formed. This poor nucleation is attributed to the lack of Sn islands observed at the film edges (Fig. 1**(f)**). The poor Nb_3Sn growth and lack Sn of islands support a low Sn concentration on the Nb(111) substrate. The lack of Sn islands may be due to the NbO/Nb(111) surface having a lower diffusivity, preventing the formation of larger Sn islands. It is likely that the Sn adatoms on Nb(111) were unable to form more thermodynamically stable clusters, resulting in extensive desorption from the surface during deposition at 850 °C. However, we also cannot rule out the possibility that a Sn monolayer may have persisted on Nb(111). The three formed domains were all similar in appearance, with the largest domain shown in Fig. 1**(e)**. The domains on Nb(111) had an intermediate average area as compared to Nb(100) or Nb(110). Overall, these observations support that Nb_3Sn growth is much less favorable on Nb(111) [22].

Table 1
Parameters changed during Nb_3Sn growth experiments.

Figure	Nb Substrate	Initial Nb Oxidation	T_{dep} (°C)	Nb_3Sn Growth Rate (nm/min)	Evaporated Sn (nm)
1	Polished Nb (100), Nb(110), & Nb(111)	Nb_2O_5	850	0.44	10
2, 3, 4	Unpolished polycrystalline Nb	Nb_2O_5 & NbO	850	0.44	10
5	Unpolished polycrystalline Nb	NbO	850 & 850 – 1100 ramp	0.44 & 4.50	10

3.2. Nb_3Sn growth on polycrystalline Nb with initial NbO or Nb_2O_5 surface

While we observed that the Nb crystallographic orientation strongly affected the Nb_3Sn nucleation and growth, realistic SRF Nb surfaces are polycrystalline and much rougher. To examine the impact of grain boundaries and surface roughness, Sn was deposited on unpolished (R_a ~ 0.09 μm) polycrystalline Nb at T_{dep}: 850 °C at 0.44 nm/min, which was the standard growth condition used in this study. Two different Nb preparation methods were used in this experiment to make low-defect

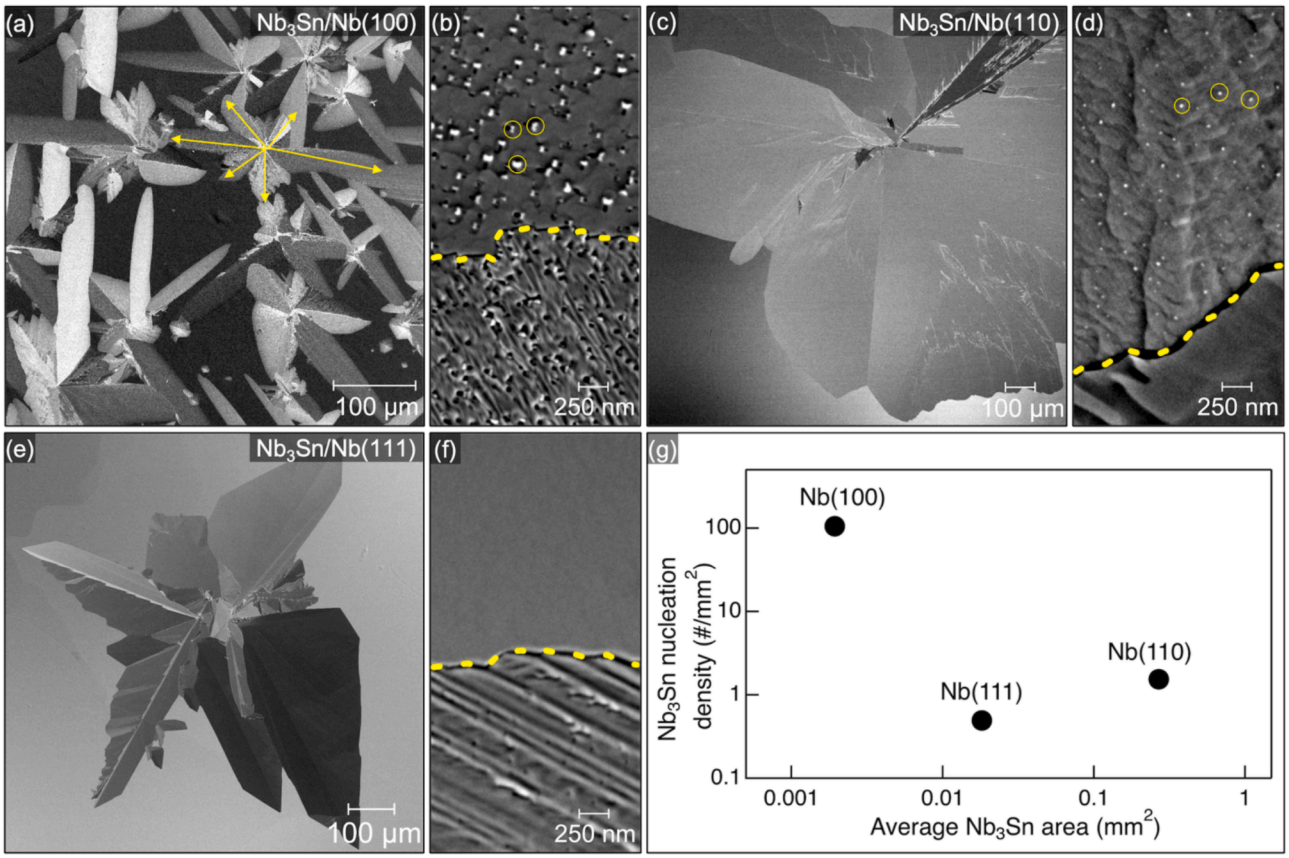

Fig. 1. Macroscale (a,c,e) and detailed (b,d,e) SEM images following Sn deposition at T_{dep}: 850 °C and 0.44 nm/min on Nb single crystals. Log scale plot (g) compares the Nb_3Sn nucleation site density (#/mm^2) and average domain size (mm^2) on Nb(1 0 0), Nb(1 1 0), and Nb(1 1 1). SEM image sizes denoted by scale bars and were obtained using the Everhart Thornley SE detector unless otherwise specified. Dotted lines represent the Nb_3Sn film edge and solid circles represent nucleated Sn islands. (a) Nb(1 0 0), yellow arrows indicate Nb_3Sn domain growth directions; (b) Nb(1 0 0); (c) Nb(1 1 0), AsB detector; (d) Nb(1 1 0); (e) Nb(1 1 1); (f) Nb(1 1 1).

and high-defect density surfaces. However, both surfaces were NbO terminated during deposition at 850 °C. The low-defect density NbO surface (Fig. 2**(a-d)**) was prepared with an initial NbO oxidation state formed from extensive high temperature UHV annealing. The more defect dense sample (Fig. 2**(e-h)**) was prepared with an *initial* native Nb_2O_5 surface that reduced to NbO during deposition at 850 °C. The initial Nb oxidation was the only procedural change between these two deposition experiments.

On both Nb polycrystalline substrates (Fig. 2**(a,e)**), the Nb_3Sn domains covered ~ 60 % of the Nb surface. Film coverage varied across each Nb grain, but surprisingly, there was no observed preferential Nb_3Sn nucleation on micron-scale Nb features or grain boundaries. The inconsistent film growth across each Nb grain is to be expected since the Nb_3Sn growth does depend on the Nb crystallographic orientation.

A higher magnification SEM of the film formed on the low-defect density NbO is shown in Fig. 2**(b)**. Unalloyed Sn islands covered the bare Nb substrate, as was the case for the Sn deposited on Nb(1 0 0) and Nb(1 1 0). Across each Nb grain, the Sn islands were uniformly distributed on the low-defect NbO surface. Fig. 2**(c)** shows a detailed image of the unalloyed Sn islands along with the Sn diameter distribution in Fig. 2**(d)**. The Sn islands have a faceted shape corresponding to a triangular-based pyramid. The morphology of these Sn islands is size dependent, conforming to a spherical shape below 100 nm. This spherical to tetrahedral shape transformation has been observed in similar sized Au FCC nanoparticles; but the geometric transformations of body-centered tetragonal metal nanoparticles, such as β-Sn, are not as well understood [35–37].

On the more defect dense Nb substrate (Fig. 2**(f)**), there is a decreasing gradient of Sn islands closer to the Nb_3Sn film edge. Furthermore, Sn islands on the more defect dense NbO have a spherical geometry (Fig. 2**(g)**) and smaller average diameter (Fig. 2**(h)**) than the islands formed on the low-defect density NbO. By comparing the differences in average Sn island size and nucleation density, it is possible to assess how the Nb substrate preparation impacts the Sn nucleation process. The high-defect density NbO surface is expected to have a higher proportion of favorable surface binding sites due to the under-coordination at step edges and other nanoscale defects [38]. Previous work of monolayer coverage Sn behavior on NbO/Nb(1 0 0) supports that variation in preferred binding sites [24,25]. The distinct surface energetics on the more defect dense NbO promote the nucleation of smaller Sn islands, similar to those observed on the Nb(1 1 0) single crystal. For these deposition conditions, the nucleation of Sn on polycrystalline Nb depends heavily on the NbO surface defect density. Therefore, any Nb pre-deposition treatments, such as annealing or pre-anodization, will affect the Nb_3Sn nucleation.

3.3. *Post-deposition annealing Nb_3Sn formed on polycrystalline Nb*

To assess the relative Sn thermal stability and Nb_3Sn degradation pathways, the Nb_3Sn films (0.44 nm Nb_3Sn/min, T_{dep}: 850 °C) formed on polycrystalline Nb, described in **Section 3.2**, underwent UHV annealing at T_{anneal}: 850, 925, 1000, and 1100 °C for 60 min each. Following each anneal, *in situ* XPS/AES spectra were taken and then the sample was removed from UHV for *ex situ* SEM/EDS analysis. Even though changing the NbO surface defect density impacted the Sn and Nb_3Sn nucleation, this did not impact the Nb_3Sn degradation process. Both Nb_3Sn films formed on polycrystalline Nb in **Section 3.2** are represented in **Sections 3.3.1 and 3.3.2**.

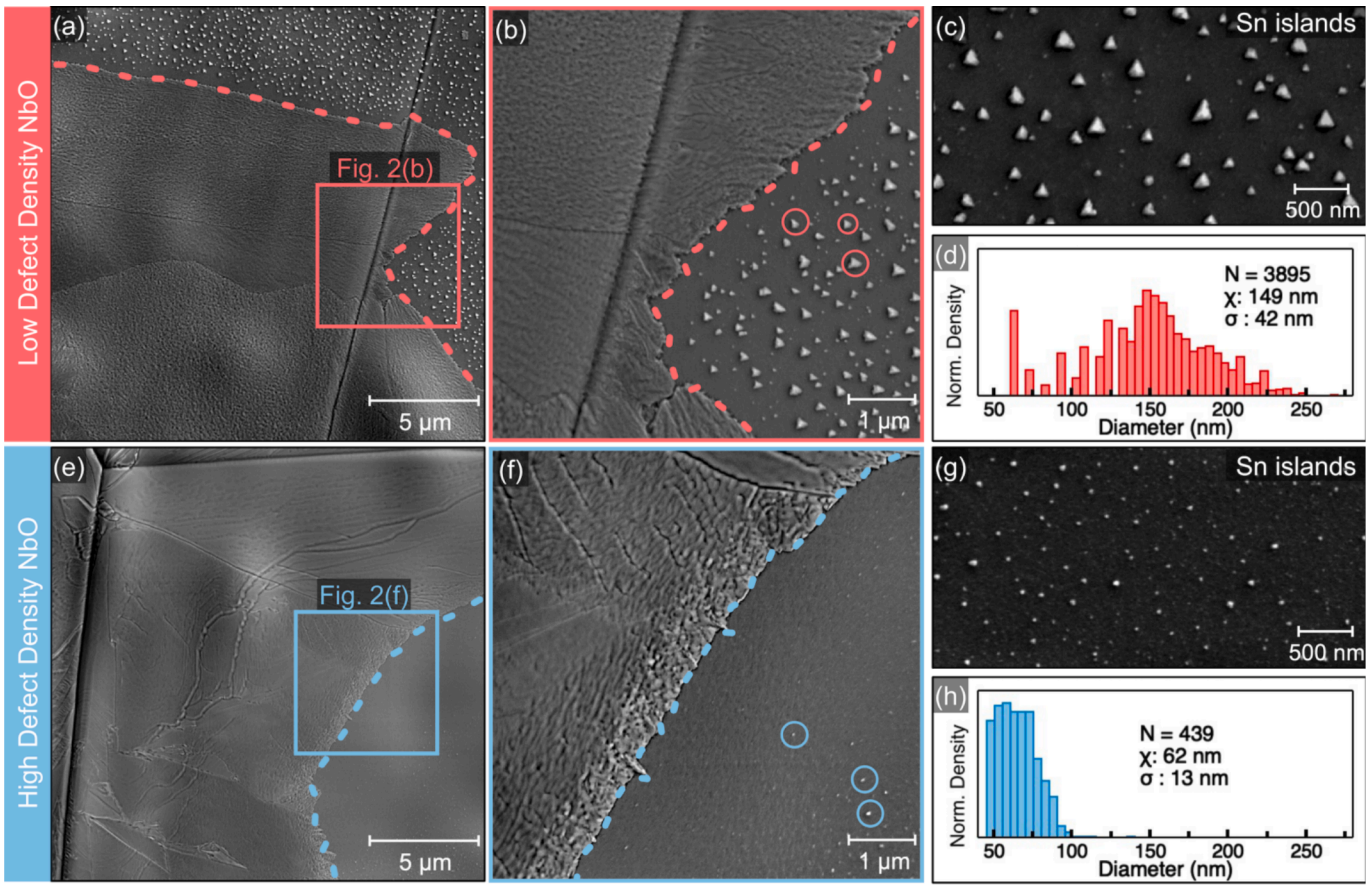

Fig. 2. SEM images of polycrystalline Nb surface following the Sn deposition at T_{dep}: 850 °C and 0.44 nm. The Nb substrate had an NbO surface during deposition with either a low (a-d) or high (e-h) surface defect density at the deposition temperature. All SEM images were taken with the Everhart Thornley SE detector and the image sizes are denoted by scale bars. Dotted lines represent the Nb_3Sn film edge and solid circles represent nucleated Sn islands. (a,e) Large scale images with visible Nb grain boundary; (b,f) higher magnification images of the regions shown by the boxes in (a,e) respectively; (c,g) Detail of unreacted Sn islands; (d, h) histograms of Sn island diameters along with each distribution sample size (N), average (χ) and standard deviation (σ).

3.3.1. *SEM and EDS of Nb_3Sn throughout degradation*

In Fig. 3, the selected SEM and EDS images are shown to represent the global trends occurring on the Nb surface following each anneal. The composition of the Sn islands was confirmed by EDS spectra that showed an increase in the Sn Lα x-ray signal and a lack of Nb Lα x-ray signal. XPS and AES data taken post-deposition confirm the lack of any additional elemental components on the surface. After the first anneal at T_{anneal}: 850 °C (Fig. 3**(a)**), the Sn islands immediately began coalescing and desorbing from the surface. The remaining Sn islands were larger and resembled irregular polyhedrons. This confirmed that the larger Sn islands had a higher thermal stability and that the Sn desorption rate was higher when annealed without a Sn overpressure. There was no sufficient evidence of extensive Nb_3Sn domain growth during the anneal at 850 °C. Rather, Nb_3Sn domains were selectively anchored to grain boundaries and other micron-scale features on the Nb substrate. Films contained a higher Sn concentration closer to the grain boundaries as shown by the inset Sn EDS map.

After annealing to T_{anneal}: 925 °C (Fig. 3**(b)**), Sn islands continued to desorb and coalesce into larger islands. Any possible new Nb_3Sn domain formation was overwhelmed by the dominant Sn precipitation rate. The EDS data showed a continued drop in Sn concentration, with the provided EDS map detailing higher Sn content near the Nb_3Sn film edge, likely due to the lateral diffusion of the nearby Sn islands. At T_{anneal}: 1000 °C (Fig. 3**(c)**), there were still Nb_3Sn domains remaining on the surface, now completely anchored to Nb grain boundaries. Only at this point, we observed Sn islands diffusing from the Nb substrate onto the Nb_3Sn film. Even though 1000 °C was well above the temperature required for Nb_3Sn formation, kinetic barriers to Sn diffusion may impede uniform growth. After T_{anneal}: 1100 °C (Fig. 3**(d)**), no Nb_3Sn domains remained on the surface. The only remaining features were large Sn islands, preferentially nestled in Nb grain boundaries.

3.3.2. *XPS spectra of oxidation during Sn desorption*

The Nb 3d, Sn 3d, and O 1 s and XPS spectra that were taken immediately following each anneal are shown in Fig. 4. XPS peaks were fitted to aid in visualizing the relative peak attenuations and the fitting details are summarized in Table 2. The dark blue spectra in Fig. 4**(a-d)** correspond to the surface immediately following Sn deposition at 850 °C. The Nb region (Fig. 4**(a)**) was fit with $3d_{5/2}$, $3d_{3/2}$ doublets representing metallic Nb, NbO, and a $Nb_xSn_yO_z$ −type oxidation state at 202.8, 203.2, and 203.9 eV respectively [39]. Each Nb $3d_{5/2}$, $3d_{3/2}$ doublet was fitted with a 3:2 peak area ratio [40]. The highest binding energy Nb 3d peak was given a general intermetallic $Nb_xSn_yO_z$ assignment as the binding energy was too low to for a NbO_2 state but distinct from the NbO binding energy. The Nb oxide XPS region is notoriously difficult to accurately fit, as the peak locations contain a high degree of overlap and are highly sensitive to contamination, which is difficult to prevent even under UHV. From the C 1 s region in Fig. 4(b), there is a minor degree of carbon contamination on the surface that gradually increases in intensity throughout the annealing procedure. The binding energy of the C 1 s contribution (284.9 eV) corresponds closest to adventitious carbon, but the lower binding energy contribution at 1100 °C may indicate trace Nb carbide formation [16,40].

The lower binding energy Sn $3d_{5/2}$, $3d_{3/2}$ doublet (Fig. 4**(c)**) had an

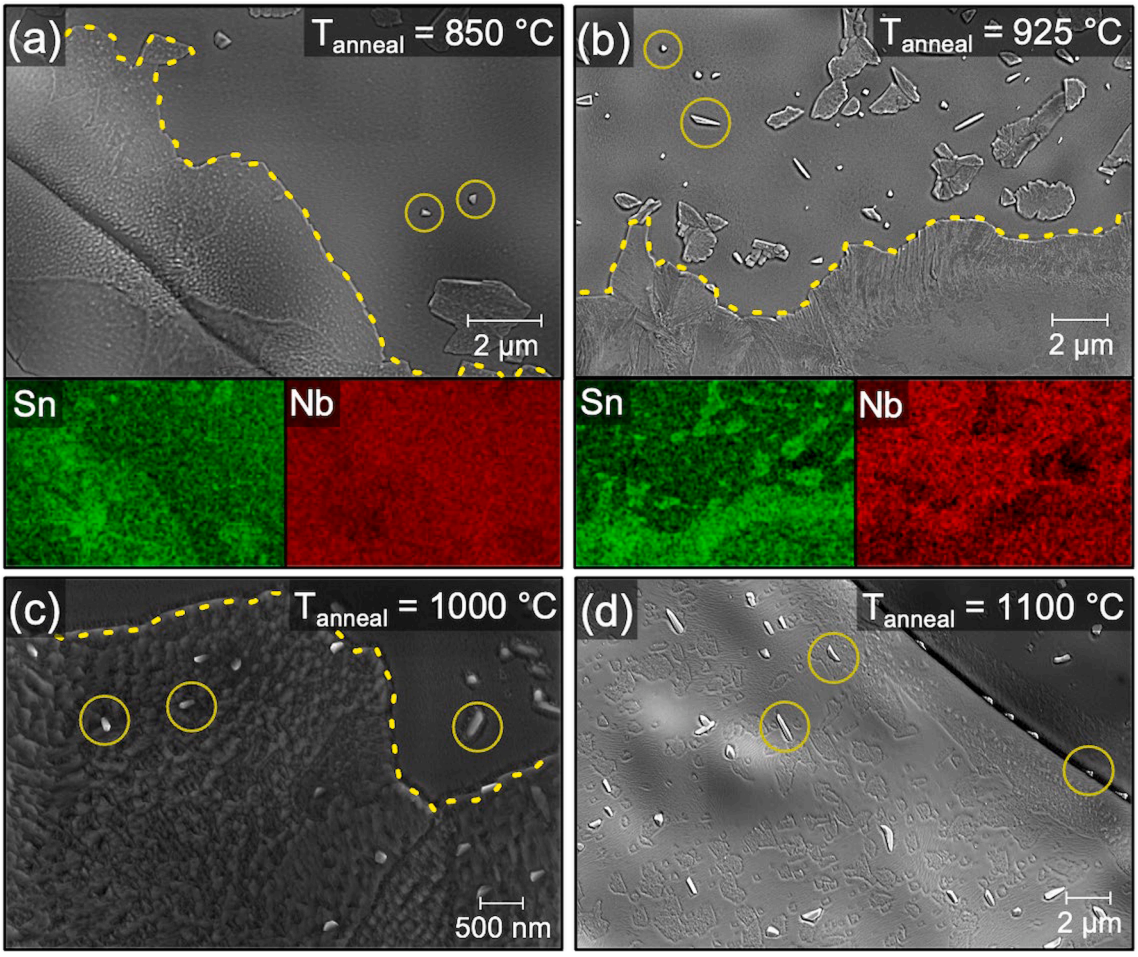

Fig. 3. SEM & EDS of Nb_3Sn/Nb surfaces following post-deposition annealing for 60 min under UHV. The Nb_3Sn was formed at T_{dep}: 850 °C and 0.44 nm/min on polycrystalline Nb. All SEM images were taken with the Everhart Thornley SE detector unless specified otherwise and the image sizes are denoted by scale bars. Dotted lines represent the Nb_3Sn film edge and solid circles represent nucleated Sn islands. (a) T_{anneal}: 850 °C, inset Nb Lα and Sn Lα EDS map; (b) T_{anneal}: 925 °C, inset Nb Lα and Sn Lα EDS map; (c) T_{anneal}: 1000 °C, SEM Inlens detector; (d) T_{anneal}: 1100 °C.

average peak binding energy at 485.0 eV and 493.47 eV corresponding to a metallic Sn state [40]. The Sn doublets were also fitted to a 3:2 peak area ratio. Once the surface was annealed, the desorption of Sn was shown as a steady decay in the Sn XPS intensity. With the signal decay, there is an accompanying Sn 3d oxide shoulder that became more prominent at higher annealing temperatures. At 1100 °C, only trace Sn remained on the surface, which was largely in a SnO_2-type oxidation state, with potentially some SnO contribution as well [41]. The Sn oxidation is supported by the growth and persistence of the O 1 s peak (Fig. 4**(d)**) after the first anneal. Due to the low intensity and broadness of the O 1 s peak, the O 1 s peak fittings do not represent specific metal oxides. By 1100 °C the surface oxygen content is comparable to clean NbO, which is to be expected as the Sn is nearly desorbed (Fig. 3**(d)**). Throughout the degradation of the Nb_3Sn film and Sn desorption process, the Nb 3d region underwent a subtle transformation, particularly with the attenuation of the higher energy $Nb_xSn_yO_z$ shoulder.

Based on these XPS data there are a few key observations to note. One is that the observed $Nb_xSn_yO_z$ species formed at the intermetallic interface is distinct from the native $Nb^{+5}Sn^{+4}O_x$ surface oxide that forms upon Nb_3Sn exposure to oxygen. The Nb_3Sn samples formed this native oxide during the *ex situ* SEM/EDS analysis. However, the annealing temperatures used in this study were well above the minimum temperatures (600–700 °C) required to reduce this native oxide [16]. The introduction of oxygen likely influences the binding energy shifts observed, but it is important to note that the desorption of Sn at these temperatures gradually exposes this oxidized Nb_3Sn/Nb interface. It is possible that the observed $Nb_xSn_yO_z$ species may have been formed at the intermetallic interface during growth and was exposed following Sn desorption. The persistence of a buried intermetallic oxide would support the role of oxygen in stabilizing Sn during the nucleation process and explain the enhanced Nb_3Sn growth on pre-anodized Nb surfaces. However, as previously mentioned, the Nb_3Sn/Nb sample was introduced to oxygen before each annealing step. This oxygen may dissolve into the Nb_3Sn film upon heating or may even precipitate from the Nb bulk. Despite the complexities involving the origin of this thermally induced $Nb_xSn_yO_z$, we can conclude that the Sn-deficient Nb_3Sn surfaces formed from annealing have distinct oxidation behavior from stoichiometric Nb_3Sn surfaces. The persistence of a Sn oxide on intermetallic surfaces has been previously demonstrated in catalytic systems, such as SnO_x/Pt and SnO_x/TiO_2 [42]. Annealing studies of these Sn-Pt and Sn-Ti surfaces show that the Sn is thermally reducible; though these Sn reduction dynamics are heavily impacted by the other intermetallic species, oxidation method, and the average size of the SnO_x islands [43,44].

3.4. Optimizing the deposition conditions on polycrystalline Nb

In **Sections 3.1-3.3**, we showed how the Nb substrate affects Sn coordination by depositing at a low Nb_3Sn growth rate and Nb deposition temperature. These conditions were selected to visualize how Nb_3Sn formation is impacted by suboptimal conditions, such as cold spots, that can occur during Sn vapor deposition in a cavity furnace. The

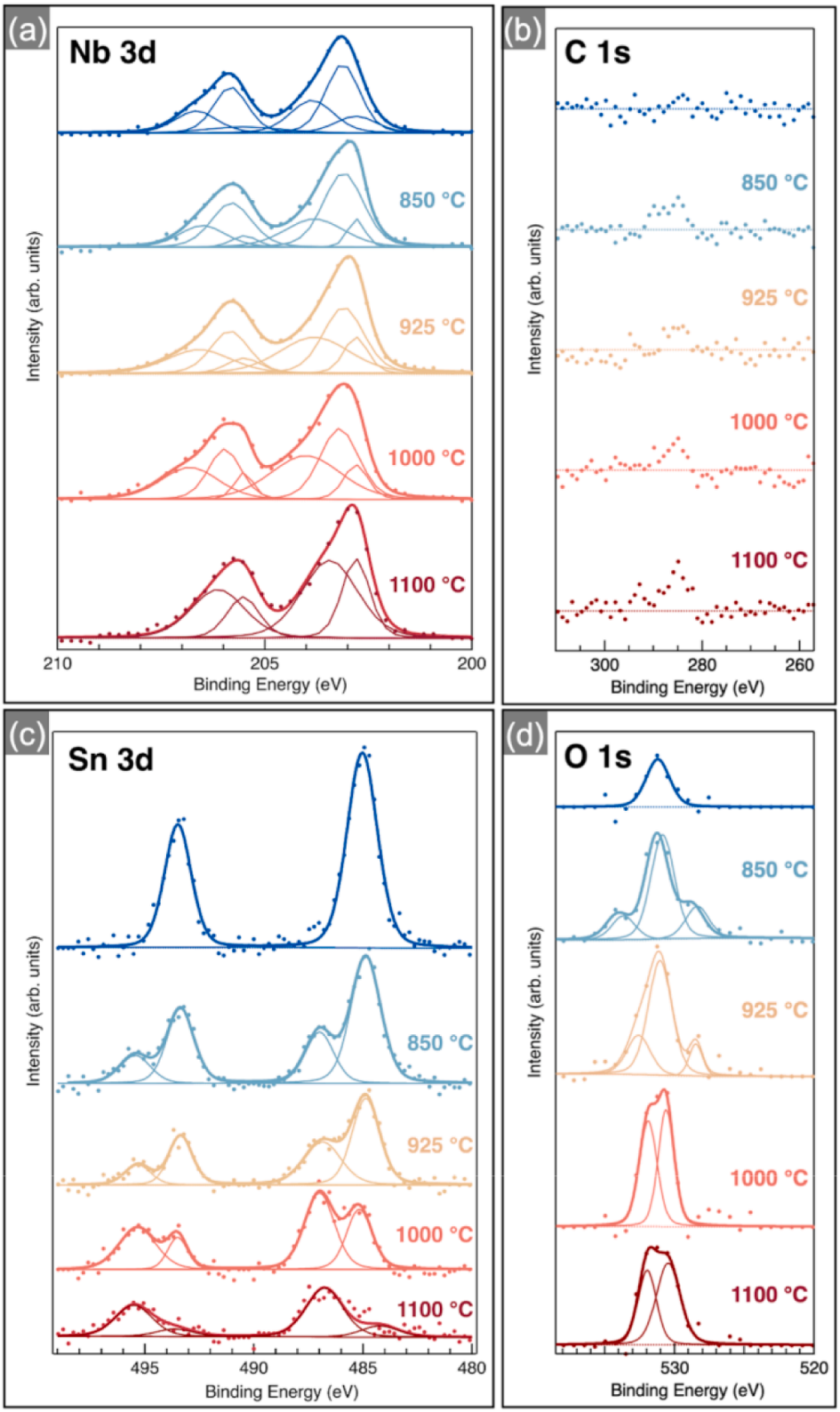

Fig. 4. Narrow window (a) Nb 3d, (b) C 1 s, (c) Sn 3d, and (d) O 1 s XPS spectra of the Nb_3Sn/Nb surfaces following deposition (dark blue) and post-deposition annealing for 60 min under UHV. The Nb_3Sn was formed at T_{dep}: 850 °C and 0.44 nm/min on polycrystalline Nb. Peak fitting of the XPS intensity (markers) is shown with the total fit (thicker lines) along with the individual peaks (thinner lines). XPS signal intensity has not been normalized or modified other than a Shirley-type background subtraction.

Table 2
Peak fitting conditions for the XPS spectra shown in Fig. 4.

XPS Peak	Chemical State (s)	Peak Energy (eV)	Doublet Split (eV)	FWHM (eV)
Nb $3d_{5/2}$	Nb	202.8 ± 0.1	2.72 ± 0.02	1.3 ± 0.8
	NbO	203.2 ± 0.1	2.73 ± 0.04	1.3 ± 0.3
	$Nb_xSn_yO_z$	203.9 ± 0.2	2.75 ± 0.05	1.3 ± 0.4
Sn $3d_{5/2}$	Sn	485.0 ± 0.1	8.46 ± 0.10	1.5 ± 0.5
	SnO_2	486.9 ± 0.2	8.49 ± 0.10	1.8 ± 0.2
O 1 s	Metal oxides, contamination	531.2 ± 2.3	–	2.0 ± 0.3

Nb_3Sn vapor deposition procedure for SRF cavities calls for a higher Nb_3Sn growth rate and Nb deposition temperature [45]. The initial Nb_3Sn nucleation at these more realistic furnace growth conditions is visualized in Fig. 5. For these experiments, Sn was deposited on polycrystalline Nb with a low-defect density NbO surface preparation. For comparison, the surface following the low 0.44 nm/min growth rate at 850 °C is shown in Fig. 5**(a)**. The film did not cover the entire substrate and the Nb_3Sn domains have an average area of 23.0 μm^2 (Fig. 5**(e)**). In Fig. 5**(b)**, the Sn was deposited at a higher growth rate of 4.5 nm/min for a shorter period of total deposition time. With the higher growth rate, the entire Nb substrate was covered by either Nb_3Sn or unreacted Sn. Increasing the growth rate did not impact the roughness of the Nb_3Sn domains, but the average area was significantly lower (Fig. 5**(f)**). The smaller Nb_3Sn domain size for the higher growth rate is due to a higher nucleation density, resulting in earlier coalescing of domains. This relationship between the deposition rate and the Nb_3Sn domain size aligns well with nucleation models for intermetallic film growth [30]. The kinetics governing intermetallic growth depend on both the nucleation and growth steps. A higher Sn deposition rate promotes the formation of smaller Sn islands. This relationship between growth rate and domain size observation is also supported by literature addressing Sn deficiencies in large Nb_3Sn grains. Following the initial formation of the Nb_3Sn domains, continued film growth is dominated by the faster Sn diffusion through Nb_3Sn grain boundaries as compared to bulk [12,45]. Therefore, a lower grain boundary density, associated with larger grain sizes, would then suffer Sn deficiencies.

Another noticeable impact of increasing the growth rate is the nucleation of drastically larger unreacted Sn islands. These larger Sn islands are faceted but have a regular polyhedral shape. These larger Sn islands are likely a consequence of the Sn deposition rate overwhelming the Nb_3Sn nucleation and growth rate; further exacerbated by the Nb_3Sn film impeding lateral diffusion of the Sn islands. The size of the Sn islands has been observed to form on Al substrate at similar conditions [46].

In Fig. 5**(c)**, the Sn flux was kept at the higher 4.50 nm/min rate and T_{dep} was gradually increased from 850 to 1100 °C throughout the deposition. For this ramped temperature experiment, the Nb_3Sn nucleation density was the highest, producing the smallest domains (Fig. 5**(g)**). There does appear to be evidence of the Nb_3Sn grains smoothing and coalescing at this higher temperature (Fig. 5**(f)**) and the large unreacted Sn islands are no longer present. This is expected, as both the Sn desorption and incorporation rate scales with sample temperature. However, the Sn atomic % at the surface (Fig. 5**(d)**) is higher for this film grown at 1100 °C. The Sn % supports that excessive Sn desorption did not occur when the surface was raised to 1100 °C. Rather, there was a more significant increase in the Sn incorporation rate. This assessment holds for situations where there is an appreciable Sn overpressure and that a substantial Sn nucleation layer has already formed. Note that it would be difficult to replicate this sort of experiment in a furnace heater, as we were able to rapidly quench both the Sn source and Nb substrate temperature within seconds. During a slower cooldown process, the surface will spend considerable periods in which Sn can accumulate and/or desorb from the film.

The Sn and O surface atomic % for each deposition type were calculated from corrected peak ratios in the differentiated Auger spectra, described elsewhere [24]. The dotted lines in Fig. 5**(d,h)** represent the noise floor limited by the signal-to-noise of the Auger spectra that were used in the calculations. The black marker represents Sn deposition on Nb at T_{dep}: 1100 °C with no temperature ramp. Regardless of the Sn flux, Nb_3Sn was unable to nucleate on polycrystalline Nb at 1100 °C. Therefore, the substrate temperature must be lower initially, to avoid excessive Sn desorption. This is reflected by the low Sn % in the Auger spectra (Fig. 5**(d)**). Since these deposited surfaces are composed of a mixture of large Sn islands and relatively rough Nb_3Sn domains, the

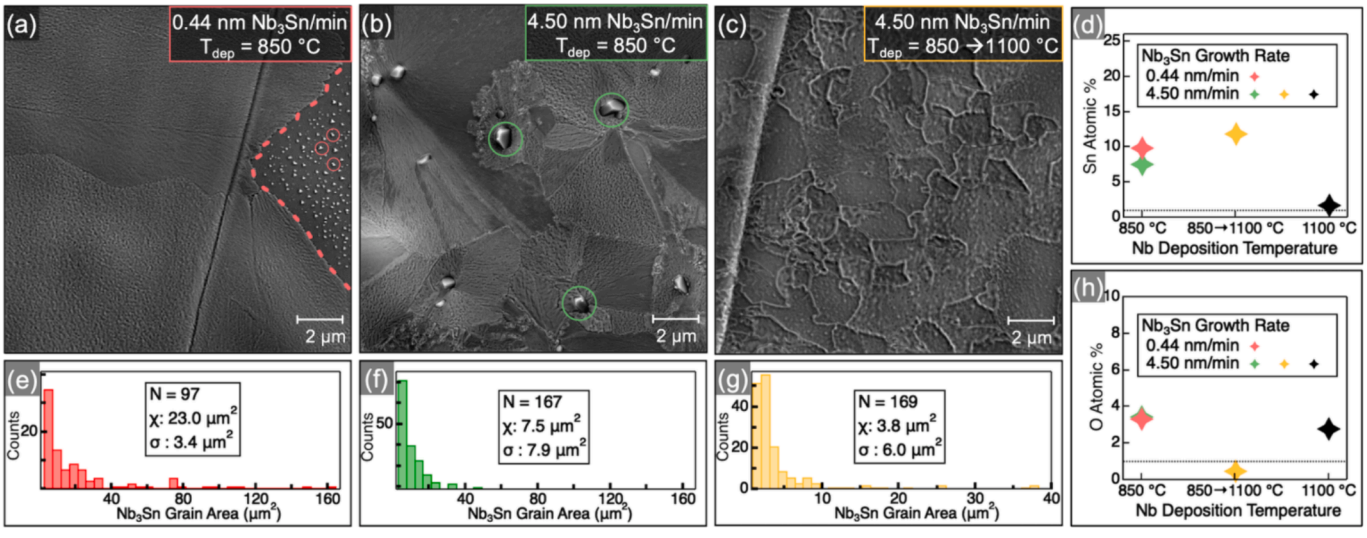

Fig. 5. SEM images (a,b,c) of Nb_3Sn grown on polycrystalline Nb substrates with varying Sn deposition conditions. All SEM images were taken with the Everhart Thornley SE detector and the image sizes are denoted by scale bars. Dotted lines represent the Nb_3Sn film edge and solid circles represent nucleated Sn islands. (e,f,g) histograms of Nb_3Sn domain areas (μm^2) corresponding to the SEM images in (a,b,c) respectively along with each distribution sample size (N), average (χ) and standard deviation (σ). (a,e) Low Sn flux (0.44 nm Nb_3Sn/min) for 60 min at T_{dep}: 850 °C; (b,f) High Sn flux (4.50 nm Nb_3Sn/min) for 6 min at T_{dep}: 850 °C; (c,g) High Sn flux (4.50 nm Nb_3Sn/min) for 6 min while gradually increasing the Nb temperature from T_{dep}: 850 to 1100 °C. Surface Sn (d) and O (h) atomic percentages calculated from *in situ* AES spectra following deposition. The horizontal dotted lines represent the noise floor for the Auger peaks. The black star in (d,h) represents Sn deposition on Nb at T_{dep}: 1100 °C where no Nb_3Sn domains formed.

extent of alloy growth cannot be described by Auger or XPS intensities alone. However, the oxygen content severely drops for the Nb_3Sn film grown at a higher deposition rate and ramped substrate temperature (Fig. 5**(h)**). This leads us to conclude that Nb_3Sn grown using the proper high growth rate and deposition temperature will not form a surface oxide in UHV. We have confirmed that the lack of a Nb_3Sn surface oxide applies to all film thicknesses ranging from the ~ 10 nm Nb_3Sn film in this study (Fig. 5**(c)**) to micron-thick films not discussed in this paper. Therefore, any surface oxygen content following deposition is due to either the exposed Nb substrate or a Sn-deficient Nb_3Sn with a higher oxidation affinity.

4. Conclusion

In this work, we examine how altering the Nb substrate properties and Sn deposition conditions impact Sn behavior and the propensity for Nb_3Sn growth. We detailed the size, spatial distribution, and morphology of the Sn islands and initial Nb_3Sn domains. In **Sections 3.1-3.3**, Nb_3Sn growth was strongly affected by the Nb substrate properties while maintaining the same deposition conditions. The distinct Sn nucleation and Nb_3Sn growth mechanisms on Nb(1 0 0), Nb(1 1 0), and Nb(1 1 1) surfaces were compared. While film growth was favorable on Nb(1 0 0) and Nb(1 1 0), the Nb_3Sn nucleation rate was significantly higher on Nb(1 0 0) whereas the growth rate of individual Nb_3Sn domains dominated on Nb(1 1 0). By examining the Nb_3Sn/Nb after the initial growth steps, we can assess how the Nb crystallographic orientations favor the formation of Nb_3Sn grains with varying sizes, smoothness, and stoichiometric homogeneity. On polycrystalline Nb substrates, we show that the Nb atomic surface features impact the nucleation thermodynamics of Sn islands and that micron-scale Nb features did not enhance Nb_3Sn formation rates. Nucleated Sn islands deposited on a more ordered NbO surface were larger than the Sn islands deposited on a more defect-dense NbO surface. The distinct geometry and sizes of nucleated Sn support our findings that the Nb substrate preparation procedure impacts Sn behavior, not because of the Nb oxidation state, but from the NbO surface binding sites that are dependent on the crystallographic orientation and temperature. In **Section 3.3** we reported on the thermally activated degradation pathways of these Nb_3Sn films formed on polycrystalline Nb. The persistence of Sn at Nb grain boundaries contextualizes how excess Sn desorption may occur throughout the vapor deposition procedure. While Sn desorption rates are always considerable while the Nb surface is heated, we discovered a site dependence of Sn desorption rates that may explain the observed Sn deficiencies in larger Nb_3Sn grains. Specifically, the Nb cavity is still $>$ 800 °C for a considerable period during the cooldown step of the vapor deposition procedure. The relatively low Sn desorption rate at Nb grain boundaries likely contributes to stoichiometric inhomogeneities in fully grown films. Furthermore, the similar desorption rates of unalloyed Sn islands and Sn in Nb_3Sn highlight the challenges associated with the removal of excess Sn residue following deposition. Finally, **Section 3.4** highlights the impact of increasing the film growth rate (0.44 → 4.50 nm/min) and deposition temperature (850 → 1100 °C) in terms of the relative Nb_3Sn domain area, Sn desorption, and Sn adatom diffusion. A higher growth rate and deposition temperature promote uniform Nb_3Sn nucleation despite the persisting growth barriers imposed by the Nb substrate atomic structure.

The Sn vapor deposition procedure is quite difficult from a thermodynamic standpoint. The Nb temperatures required for the A15 Nb_3Sn structure to form are quite high; the threshold for promoting homogeneous Sn diffusion is even higher. The extent of Sn desorption at these temperatures is difficult to suppress. The formation of a pristine Nb_3Sn film requires the assurance that a homogeneous intermetallic interface was able to form during the nucleation step. The surface reactions that take place during the first few hours of the deposition procedure are critical. While $SnCl_2$ agents may aid in supporting Sn on Nb surfaces, further work is necessitated to understand the thermodynamics of why Sn adatoms are not stable on Nb at these conditions. Our results provide evidence for the NbO surface serving as an energetic blockade against Nb_3Sn nucleation. These reported findings visualized Nb_3Sn during the initial growth steps and serve to both inform and validate ongoing efforts to optimize the vapor deposition procedure for improved SRF cavities.

CRediT authorship contribution statement

Sarah A. Willson: Writing – review & editing, Writing – original draft, Visualization, Validation, Methodology, Investigation, Formal analysis, Data curation, Conceptualization. **Helena Lew-Kiedrowska:** Investigation, Formal analysis. **Van Do:** Writing – review & editing, Visualization, Investigation. **S.J. Sibener:** Writing – review & editing, Supervision, Resources, Project administration, Methodology, Funding acquisition, Conceptualization.

Declaration of competing interest

The authors declare that they have no known competing financial interests or personal relationships that could have appeared to influence the work reported in this paper.

Data availability

Data will be made available on request.

Acknowledgments

This work was supported by the U.S. National Science Foundation under Award PHY-1549132, the Center for Bright Beams. Infrastructure and facilities from the NSF Materials Research Science and Engineering Center (MRSEC) at the University of Chicago, Grant No. NSF-DMR-2011854, are also acknowledged.

References

[1] H. Padamsee, R.F. Superconductivity, Science, Technology, and Applications, 1st ed., Wiley, New York, 2009.
[2] H. Padamsee, J. Knobloch, RF Superconductivity for Accelerators, 2nd ed., Wiley, New York, 2008.
[3] C. Antoine, Materials and surface aspects in the development of SRF Niobium cavities, in: Proc. EuCARD Editorial Series on Accelerator Science, EuCARD-BOO-2012-001, Warsaw, Poland, 2012.
[4] S. Posen, M. Liepe, Advances in development of Nb_3Sn superconducting radio-frequency cavities, Phys. Rev. Spec. Top. - Accel. Beams 17 (2014) 112001, https://doi.org/10.1103/PhysRevSTAB.17.112001.
[5] A. Godeke, A review of the properties of Nb_3Sn and their variation with A15 composition, morphology and strain state, Supercond. Sci. Technol. 19 (2006) R68–R80, https://doi.org/10.1088/0953-2048/19/8/R02.
[6] S. Posen, M. Liepe, D.L. Hall, Proof-of-principle demonstration of Nb_3Sn superconducting radiofrequency cavities for high Q0 applications, Appl. Phys. Lett. 106 (2015) 082601, https://doi.org/10.1063/1.4913247.
[7] U. Pudasaini, G.V. Eremeev, J.W. Angle, J. Tuggle, C.E. Reece, M.J. Kelley, Growth of Nb_3Sn coating in tin vapor-diffusion process, J. Vac. Sci. Technol. A 37 (2019) 051509, https://doi.org/10.1116/1.5113597.
[8] R.D. Porter, D.L. Hall, M. Liepe, J.T. Maniscalco, C. University, Surface Roughness Effect on the Performance of Nb_3Sn Cavities, in: Proc. of LINAC2016, East Lansing, MI, 2017, Vol. 4, pp 129−13, JACoW.
[9] M.M. Kelley, N.S. Sitaraman, T.A. Arias, Ab initio theory of the impact of grain boundaries and substitutional defects on superconducting Nb_3Sn, Supercond. Sci. Technol. 34 (2020) 015015, https://doi.org/10.1088/1361-6668/abc8ce.
[10] S. Posen, J. Lee, D.N. Seidman, A. Romanenko, B. Tennis, O.S. Melnychuk, D. A. Sergatskov, Advances in Nb_3Sn superconducting radiofrequency cavities towards first practical accelerator applications, Supercond. Sci. Technol. 34 (2021) 025007, https://doi.org/10.1088/1361-6668/abc7f7.
[11] G. Jiang, S. Wu, Z. Yang, Y. He, Y. Ye, H. Guo, C. Li, P. Xiong, L. Li, S. Huang, A. Wu, F. Qiu, J. Zhang, X. Niu, Q. Huang, Z. Qin, T. Tan, Z. Wang, S. Zhang, H. Zhao, W. Zhan, Understanding and optimization of the coating process of the radio-frequency Nb_3Sn thin film superconducting cavities using tin vapor diffusion method, Appl. Surf. Sci. 643 (2024) 158708, https://doi.org/10.1016/j.apsusc.2023.158708.
[12] T. Spina, B.M. Tennis, J. Lee, D.N. Seidman, S. Posen, Development and Understanding of Nb_3Sn films for radiofrequency applications through a sample-

host 9-cell cavity, Supercond. Sci. Technol. 34 (2020) 015008, https://doi.org/10.1088/1361-6668/abbec4.
[13] U. Pudasaini, C. Reece, J. Tiskumara, Managing Sn-supply to tune surface characteristics of vapor-diffusion coating of Nb_3Sn, in: Proc. of 20th Int. Conf. RF Supercond. East Lansing, MI, USA, 2021. DOI: 10.2172/1905472.
[14] J. Tiskumara, J. Delayen, G. Eremeev, U. Pudasaini, C. Reece, Nb_3Sn Coating of Twin Axis Cavity for SRF Applications, in: Proc. of 20th Int. Conf. RF Supercond. East Lansing, MI, USA, 2021, 146-150, SUPTEV011.
[15] J. Tiskumara, J. Delayen, G. Eremeev, U. Pudasaini, Lower Temperature Annealing of Vapor Diffused Nb_3Sn for Accelerator Cavities, in: Proc. of 5th North Am. Part. Accel. Conf. Albuquerque, NM, USA, 2022, 695-698, WEPA31.
[16] A. Cano, G.V. Eremeev, J.R. Zuazo, J. Lee, B. Luo, M. Martinello, A. Romanenko, S. Posen, Selective Thermal Evolution of a Native Oxide Layer in Nb and Nb_3Sn-Coated SRF Grade Nb: An In Situ XPS Study, J. Phys. Chem. C 127 (2023) 19705–19716, https://doi.org/10.1021/acs.jpcc.3c03108.
[17] Z. Sun, D.K. Dare, Z. Baraissov, D.A. Muller, M.O. Thompson, M.U. Liepe, Thermodynamic route of Nb_3Sn nucleation: Role of oxygen, APL Mater. 11 (2023) 071118, https://doi.org/10.1063/5.0157659.
[18] H. Oechsner, J. Giber, H.J. Füßer, A. Darlinski, Phase transition and oxide dissolution processes in vacuum-annealed anodic Nb_2O_5/Nb systems, Thin Solid Films 124 (1985) 199–210, https://doi.org/10.1016/0040-6090(85)90266-4.
[19] B.R. King, H.C. Patel, D.A. Gulino, B.J. Tatarchuk, Kinetic measurements of oxygen dissolution into niobium substrates: In situ X-ray photoelectron spectroscopy studies, Thin Solid Films 192 (1990) 351–369, https://doi.org/10.1016/0040-6090(90)90079-S.
[20] R.D. Veit, N.A. Kautz, R.G. Farber, S.J. Sibener, Oxygen dissolution and surface oxide reconstructions on Nb(100), Surf. Sci. 688 (2019) 63–68, https://doi.org/10.1016/j.susc.2019.06.004.
[21] J. Halbritter, ARXPS analysis and oxidation of niobium compounds, Electrochimica Acta 34 (1989) 1153–1155, https://doi.org/10.1016/0013-4686(89)87149-X.
[22] B. Hillenbrand, Y. Uzel, K. Schnitzke, On the preparation of Nb_3Sn-layers on monocrystalline Nb-substrates, Appl. Phys. 23 (1980) 237–240, https://doi.org/10.1007/BF00914905.
[23] J.A. Venables, G.D.T. Spiller, M. Hanbucken, Nucleation and growth of thin films, Rep. Prog. Phys. 47 (1984) 399, https://doi.org/10.1088/0034-4885/47/4/002.
[24] S.A. Willson, R.G. Farber, A.C. Hire, R.G. Hennig, S.J. Sibener, Submonolayer and Monolayer Sn Adsorption and Diffusion Behavior on Oxidized Nb(100), J. Phys. Chem. C 127 (2023) 3339–3348, https://doi.org/10.1021/acs.jpcc.2c08458.
[25] R.G. Farber, S.A. Willson, S.J. Sibener, Role of nanoscale surface defects on Sn adsorption and diffusion behavior on oxidized Nb(100), J. Vac. Sci. Technol. A 39 (2021) 063212, https://doi.org/10.1116/6.0001374.
[26] B. An, S. Fukuyama, K. Yokogawa, M. Yoshimura, Surface structures of clean and oxidized Nb(100) by LEED, AES, and STM, Phys. Rev. B 68 (2003) 115423, https://doi.org/10.1103/PhysRevB.68.115423.
[27] K. Zhussupbekov, K. Walshe, S.I. Bozhko, A. Ionov, K. Fleischer, E. Norton, A. Zhussupbekova, V. Semenov, I.V. Shvets, B. Walls, Oxidation of Nb(110): atomic structure of the NbO layer and its influence on further oxidation, Sci. Rep. 10 (2020) 3794, https://doi.org/10.1038/s41598-020-60508-2.
[28] A.A. McMillan, J.D. Graham, S.A. Willson, R.G. Farber, C.J. Thompson, S. J. Sibener, Persistence of the Nb(100) surface oxide reconstruction at elevated temperatures, Supercond. Sci. Technol. 33 (2020) 105012, https://doi.org/10.1088/1361-6668/abaec0.
[29] M.D. Michiel, C. Scheuerlein, Phase transformations during the reaction heat treatment of powder-in-tube Nb_3Sn superconductors, Supercond. Sci. Technol. 20 (2007) L55, https://doi.org/10.1088/0953-2048/20/10/L01.
[30] R. Donald, Askeland, The Science and Engineering of Materials, 6th ed., Cengage, Stamford, CT, USA, 2010.
[31] K. Shirzad, C. Viney, A critical review on applications of the Avrami equation beyond materials science, J. R. Soc. Interface. 20 (2023) 20230242, https://doi.org/10.1098/rsif.2023.0242.
[32] M. Ohring, The Material Science of Thin Films, Academic Press, San Diego, CA, 1992.
[33] S. Pal, K.A. Fichthorn, Size dependence of the diffusion coefficient for large adsorbed clusters, Phys. Rev. B 60 (1999) 7804–7807, https://doi.org/10.1103/PhysRevB.60.7804.
[34] C. DeW, Van Siclen, Single Jump Mechanisms for Large Cluster Diffusion on Metal Surfaces, Phys. Rev. Lett. 75 (1995) 1574–1577, https://doi.org/10.1103/PhysRevLett.75.1574.
[35] Y. Zheng, W. Liu, T. Lv, M. Luo, H. Hu, P. Lu, S.-I. Choi, C. Zhang, J. Tao, Y. Zhu, Z.-Y. Li, Y. Xia, Seed-Mediated Synthesis of Gold Tetrahedra in High Purity and with Tunable, Well-Controlled Sizes, Chem. Asian J. 9 (2014) 2635–2640, https://doi.org/10.1002/asia.201402499.
[36] Q.N. Nguyen, C. Wang, Y. Shang, A. Janssen, Y. Xia, Colloidal Synthesis of Metal Nanocrystals: From Asymmetrical Growth to Symmetry Breaking, Chem. Rev. 123 (2023) 3693–3760, https://doi.org/10.1021/acs.chemrev.2c00468.
[37] C. Boukouvala, E.R. Hopper, D.M. Kelly, P.J. Knight, J.S. Biggins, E. Ringe, Beyond Simple Crystal Systems: Identifying Twinning in Body-Centered Tetragonal Nanoparticles, Cryst. Growth Des. 22 (2022) 653–660, https://doi.org/10.1021/acs.cgd.1c01188.
[38] Z. Zhang, M.G. Lagally, Atomistic Processes in the Early Stages of Thin-Film Growth, Science 276 (1997) 377–383, https://doi.org/10.1126/science.276.5311.377.
[39] Z.P. Hu, Y.P. Li, M.R. Ji, J.X. Wu, The interaction of oxygen with niobium studied by XPS and UPS, Solid State Commun. 71 (1989) 849–852, https://doi.org/10.1016/0038-1098(89)90210-X.
[40] J.F. Moulder, Handbook of X-ray Photoelectron Spectroscopy: A Reference Book of Standard Spectra for Identification and Interpretation of XPS Data, Perkin-Elmer Corporation Physical Electronics Division, Eden Prairie, MN, 1992.
[41] M.A. Stranick, A. Moskwa, SnO_2 by XPS, Surf. Sci. Spectra 2 (1993) 50–54, https://doi.org/10.1116/1.1247724.
[42] S. Beniwal, W. Chai, K. Metavarayuth, T.D. Maddumapatabandi, D.M. Shakya, G. Henkelman, D.A. Chen, Oxidation of Sn at the Cluster-Support Interface: Sn and Pt–Sn Clusters on TiO2(110), J. Phys. Chem. C 125 (2021) 17671–17683, https://doi.org/10.1021/acs.jpcc.1c03338.
[43] M. Batzill, D.E. Beck, D. Jerdev, B.E. Koel, Tin-oxide overlayer formation by oxidation of Pt–Sn(111) surface alloys, J. Vac. Sci. Technol. A 19 (2001) 1953–1958, https://doi.org/10.1116/1.1345902.
[44] N.A. Saliba, Y.-L. Tsai, B.E. Koel, Oxidation of Ordered Sn/Pt(111) Surface Alloys and Thermal Stability of the Oxides Formed, J. Phys. Chem. B 103 (1999) 1532–1541, https://doi.org/10.1021/jp983523q.
[45] J. Lee, S. Posen, Z. Mao, Y. Trenikhina, K. He, D.L. Hall, M. Liepe, D.N. Seidman, Atomic-scale analyses of Nb_3Sn on Nb prepared by vapor diffusion for superconducting radiofrequency cavity applications: a correlative study, Supercond. Sci. Technol. 32 (2018) 024001, https://doi.org/10.1088/1361-6668/aaf268.
[46] C. Eisenmenger-Sittner, H. Bangert, H. Störi, J. Brenner, P.B. Barna, Stranski-Krastanov growth of Sn on a polycrystalline Al film surface initiated by the wetting of Al by Sn, Surf. Sci. 489 (2001) 161–168, https://doi.org/10.1016/S0039-6028(01)01174-8.